energies

MDPI

Article

Single Three-Phase Inverter for Dual-Frequency Induction Heating

Krystian Frania [1,*], Kamil Kierepka [2], Marcin Kasprzak [1] and Piotr Zimoch [3]

[1] Department of Power Electronics, Electrical Drivers and Robotics, Silesian University of Technology, 44-100 Gliwice, Poland; marcin.kasprzak@polsl.pl
[2] TRUMPF Huettinger, 05-220 Zielonka, Poland; kamil.kierepka@trumpf.com
[3] TechFirm Industrie AG, 8001 Zürich, Switzerland; piotr.zimoch@polsl.pl
* Correspondence: krystian.frania@polsl.pl

Abstract: This paper presents new resonant inverter topologies for dual-frequency induction heating (IH). These 2T1C and 3T topologies combine the advantageous features of two- and one-inverter solutions. An analytical description of the load impedance of a dual-frequency series-parallel circuit has been made. Using manufacturer datasheets and LTspice models of selected transistors, a MATLAB model was parameterized. Based on it, power losses are determined as a function of the following parameters: nominal power, frequency and DC bus voltage. The obtained results allowed for determining the data necessary in the design process. The research has been experimentally verified. Tests were carried out for pulsing and simultaneous operation. Power control characteristics as a function of frequency are determined. The possibility of operating the inverter with high efficiency (>97%) in the proposed 2T1C and 3T systems at nominal power is demonstrated.

Keywords: gear hardening; frequency modulation (FM); SiC power MOSFETs; resonant power conversion

Citation: Frania, K.; Kierepka, K.; Kasprzak, M.; Zimoch, P. Single Three-Phase Inverter for Dual-Frequency Induction Heating. *Energies* **2024**, *17*, 2489. https://doi.org/10.3390/en17112489

Academic Editor: Federico Barrero

Received: 18 April 2024
Revised: 18 May 2024
Accepted: 19 May 2024
Published: 22 May 2024

1. Introduction

Research on induction heating (IH) dates back to the 19th century. In 1887, Sebastian de Ferranti, an English electrical engineer, proposed an induction furnace for metal melting [1]. In recent decades, IH systems have found many practical applications and have become a subject of intense research. They are mainly applied in industry [2–4], domestic applications [5–7] and medicine [8–10]. IH technology has been an increasingly attractive research area due to advantages over conventional heating methods [11–13]. These are mainly faster heating times, improved safety and higher efficiency.

A common case encountered in industry is the need to improve the mechanical properties of irregularly shaped components, such as gears. Depending on the application, different surface hardness profiles of the gear wheel are required. Modeling the hardness profiles of gears is problematic, mainly due to the different couplings between the inductor and the root and teeth areas. In addition, there is significant heat transfer from around the roots into the gear. The parameters that have a significant effect on obtaining the desired hardness profiles are frequency, power, cycle time, inductor geometry and cooling conditions. Obtaining a uniform temperature distribution is closely related to the penetration depth of the eddy currents [14]. This depth decreases as the frequency of the inductor current increases. The eddy current (and indirectly temperature) distributions for heating with a high-frequency (HF) current, a medium-frequency (MF) current and a current with both HF and MF components are indicated in Figure 1.

The four basic concepts of induction hardening of gears are shown in Figure 2. They are as follows [15,16]:

- Conventional single frequency (CSF). It is used for small- and medium-sized gears.
- Pulsing single frequency (PSF). The heating process is divided into two parts. The first one is longer and is a pre-heat. It is performed at a lower power, allowing the heat

flow to reach the root without overheating the teeth at the same time. The second one is a post-heat, which is performed at a much higher power and in a much shorter time.

- Pulsing dual frequency (PDF). It is similar to the previous one. Pre-heating is carried out when the inductor is supplied with an MF current. HF current and much higher power are used for post-heating.
- Simultaneous dual frequency (SDF). It is characterized by the fact that the inductor is supplied with a current with two components, HF and MF, simultaneously. The hardening process can be carried out in different ways. It is possible to adjust the on/off times of individual components, as well as their power.

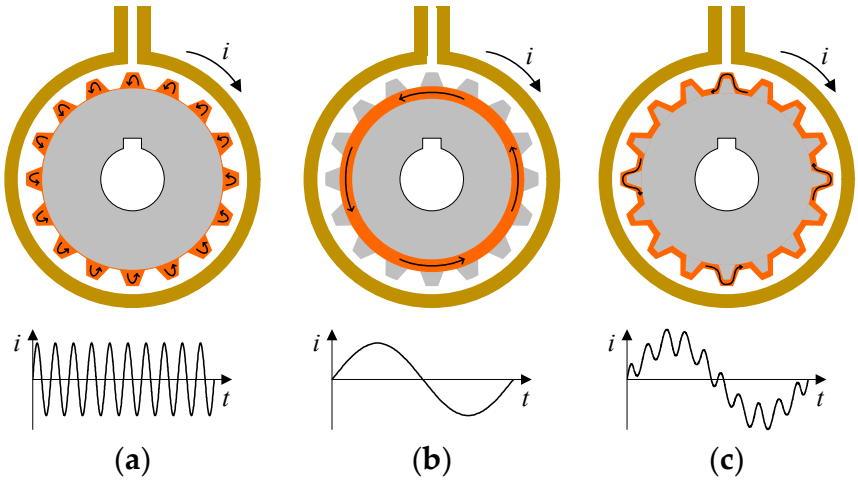

Figure 1. Distribution of eddy currents in a gear wheel for components (**a**) HF, (**b**) MF and (**c**) HF+MF.

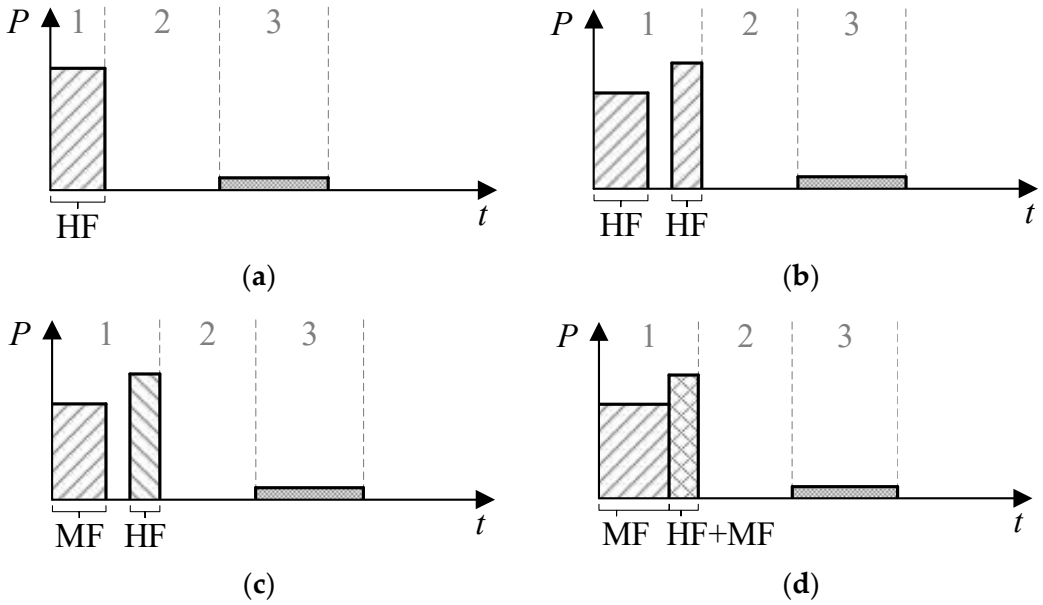

Figure 2. Methods for induction hardening of gears (1—heating, 2—quenching, 3—tempering): (**a**) CSF; (**b**) PSF; (**c**) PDF; (**d**) SDF.

Based on these concepts, it can be assumed that the ability to generate mono- and poly-harmonic currents is needed. The dual-frequency inverter solutions for IH presented in the literature and patent claims can be divided into two groups. The first are complex systems with two inverters [17,18], and the second are simple systems with one inverter [19]. The complex systems consist of two separate voltage source inverters with outputs connected to independent matching transformers. The secondary sides of the matching transformers are equipped with HF and MF resonant circuits, respectively. This solution is characterized by flexibility due to the possibility of controlling individual frequency components of the inductor current. In addition, it is possible to adjust the load impedance minima independently by changing the transformers' turns ratios. The simpler systems consist of one voltage source inverter with the output connected to a matching transformer. The secondary side of the matching transformer is equipped with a dual-frequency resonant circuit. This solution is characterized by simplicity but also by mismatching the load impedance minima related to the occurrence of series resonances [20–22]. In addition, there are solutions with one inverter without matching transformers, but in this case, there is also a mismatch of load impedance minima [23]. The above solutions allow operation in pulsing and simultaneous modes. There are also solutions that allow dual-frequency IH in pulsing mode only [24].

The novelty of this article is the proposal of new resonant inverter topologies for dual-frequency IH. These 2T1C and 3T topologies combine the advantageous features of two- and one-inverter solutions, i.e., the ability to control individual components of the inductor current and independently adjust the load impedance minima (independent matching transformers), as well as simplicity. Both proposed topologies are protected by Polish patent claims [25,26]. A comparison of the basic properties of these and similar systems for dual-frequency IH covered by the patent claims is shown in Table 1.

Table 1. Systems for dual-frequency IH presented in the patent claims.

Patent No.	System Type	Independent Control of HF and MF Components	Load Impedance Matching for the Components HF and MF
EP1363474A2	complex	Yes	Yes
EP2147983A1	complex	Yes	Yes
EP2148551A1	simple	No	No
PL241666B1	simple	Yes	Yes
PL439134A1	simple	Yes	Yes

The remainder of this paper is organized as follows. Firstly, the proposed 2T1C and 3T topologies of dual-frequency inverters are presented in Section 2. Considering the proposed application and system properties, the load impedance of a dual-frequency series-parallel circuit is analyzed in Section 3. Based on manufacturer datasheets and LTspice models of selected transistors, a MATLAB (R2021b) model is parameterized in Section 4, which allows the determination of power losses. Section 5 presents the main implementation and experimental results proving proper operation. Finally, the main conclusions of this paper are summarized in Section 6.

2. Proposed Dual-Frequency Inverter Topologies

Two inverter topologies are proposed. The following designations of 2T1C [25] and 3T [26] are adopted in this paper. The 2T1C topology shown in Figure 3 contains two transistor branches (2T) and one common capacitor branch (1C), which can be used to eliminate the DC component. The first branch controlled by the signal s_1 is responsible for generating the MF component, while the second branch controlled by the signal s_2 is responsible for generating the HF component. Transformers Tr_1 and Tr_2 are used to match the load impedance minima independently for each component. Passive elements L_1, C_1 and L_2, C_2 are used to set the frequencies of the MF and HF components, respectively. This topology allows for pulsing operation mode when the inductor current i contains only

one of the components (MF or HF) and simultaneous operation mode when the inductor current i contains both components (MF+HF). An important feature of the 2T1C topology is that the rms value of the inverter output voltage (v_1, v_2) is the same for each component in each operating mode.

The 3T topology is presented in Figure 4. Compared to the 2T1C topology, in the 3T topology the common capacitor branch has been replaced by a transistor branch. This branch controlled by the signal s_3, depending on the operation mode, can be switched with the frequency of the MF or HF component. An important feature of the 3T topology is the equal rms value of the inverter output voltage (v_1, v_2) for each component during pulsing operation mode. For simultaneous operation mode, the rms value of v_1 voltage for the MF component is twice that of v_2 voltage for the HF component.

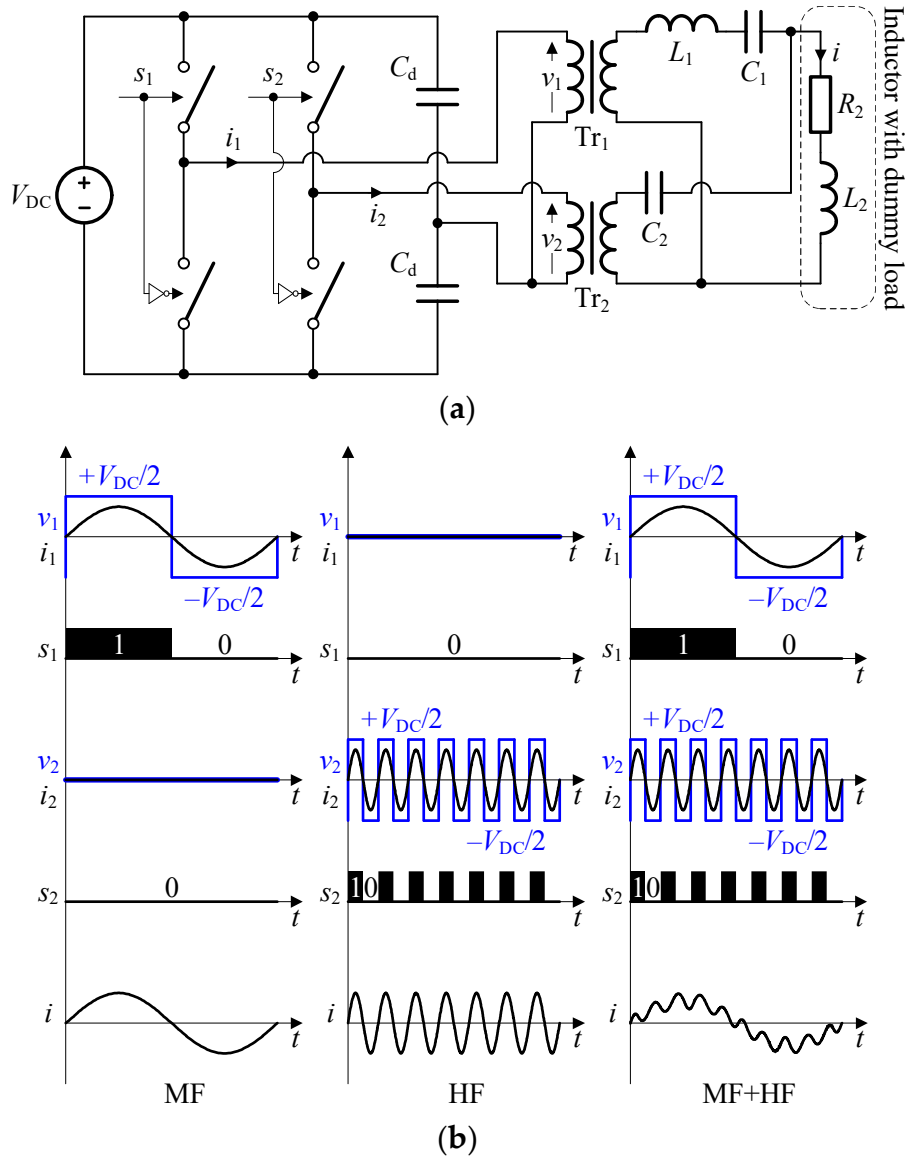

Figure 3. 2T1C topology: (**a**) circuit diagram; (**b**) waveforms for MF, HF and MF+HF operation.

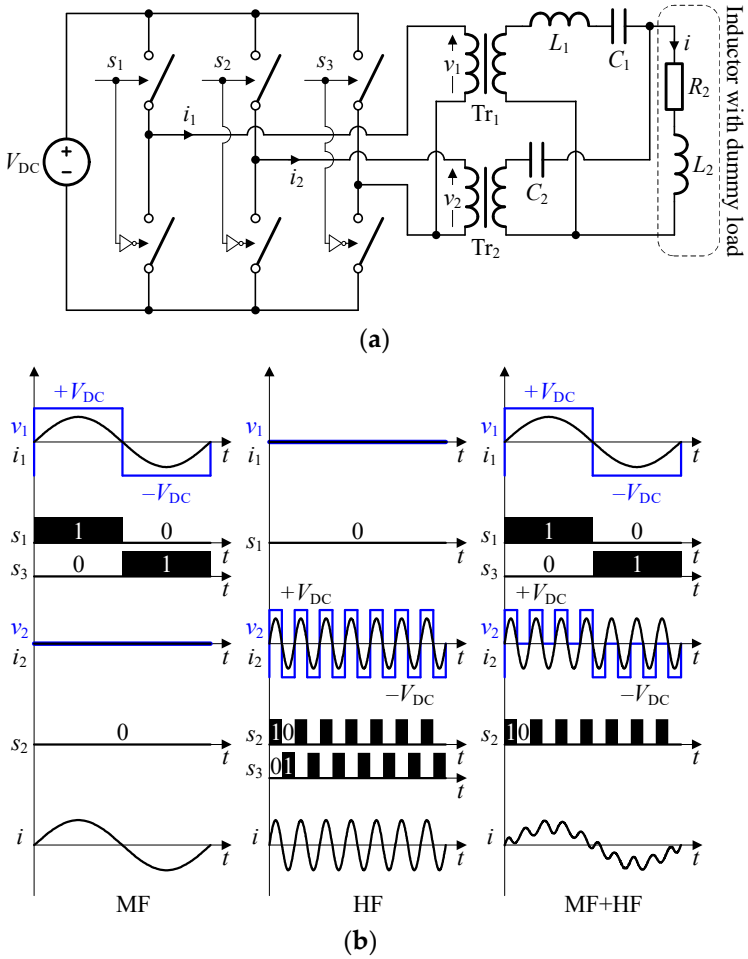

Figure 4. 3T topology: (**a**) circuit diagram; (**b**) waveforms for MF, HF and MF+HF operation.

3. Analytical Model of the Inverter Load

The topology of a dual-frequency load circuit is shown in Figure 5. Each component of the normalized equivalent impedance $Z^\bullet$ (1) is related to the characteristic impedance Z_{02}, which is calculated from L_2 and C_2. This reference makes it easier to interpret changes in the quality factor Q_2 (2). These changes are mainly due to the change in the equivalent resistance R_2 of the inductor-load circuit. The circuit can be analyzed as a combination of two series of resonant circuits $R_1L_1C_1$ and $R_2L_2C_2$. The resonant angular frequencies ω_{01}, ω_{02} of each sub-circuit are determined by (3). The coefficients k_R, k_L and k_C (4) are used in (1) to define the relationships of the parameters of each sub-circuit. Furthermore, the resistive elements (i.e., the parasitic resistance R_1 of the inductor L_1 and the equivalent resistance R_2 of the inductor-load circuit) in the model are described, considering the frequency impact due to skin effect [14].

$$Z^\bullet = \frac{\left(\frac{k_\mathrm{R}\sqrt{\omega^\bullet}}{Q_2} + \mathrm{j}\frac{\omega^\bullet k_\mathrm{L}}{\sqrt{k_\mathrm{L}k_\mathrm{C}}} - \mathrm{j}\frac{\sqrt{k_\mathrm{L}k_\mathrm{C}}}{\omega^\bullet k_\mathrm{C}}\right)\left(-\mathrm{j}\frac{\sqrt{k_\mathrm{L}k_\mathrm{C}}}{\omega^\bullet}\right)}{\frac{k_\mathrm{R}\sqrt{\omega^\bullet}}{Q_2} + \mathrm{j}\frac{\omega^\bullet k_\mathrm{L}}{\sqrt{k_\mathrm{L}k_\mathrm{C}}} - \mathrm{j}\frac{\sqrt{k_\mathrm{L}k_\mathrm{C}}}{\omega^\bullet k_\mathrm{C}} - \mathrm{j}\frac{\sqrt{k_\mathrm{L}k_\mathrm{C}}}{\omega^\bullet}} + \frac{\sqrt{\omega^\bullet}}{Q_2} + \mathrm{j}\frac{\omega^\bullet}{\sqrt{k_\mathrm{L}k_\mathrm{C}}} \tag{1}$$

$$Q_2 = \frac{\omega_{02}L_2}{R_2} = \frac{1}{\omega_{02}C_2R_2} \tag{2}$$

$$\omega_{01} = \frac{1}{\sqrt{L_1C_1}},\ \omega_{02} = \frac{1}{\sqrt{L_2C_2}},\ \omega^\bullet = \frac{\omega}{\omega_{01}} \tag{3}$$

$$k_\mathrm{R} = \left.\frac{R_1}{R_2}\right|_{\omega^\bullet=1},\ k_\mathrm{L} = \frac{L_1}{L_2},\ k_\mathrm{C} = \frac{C_1}{C_2} \tag{4}$$

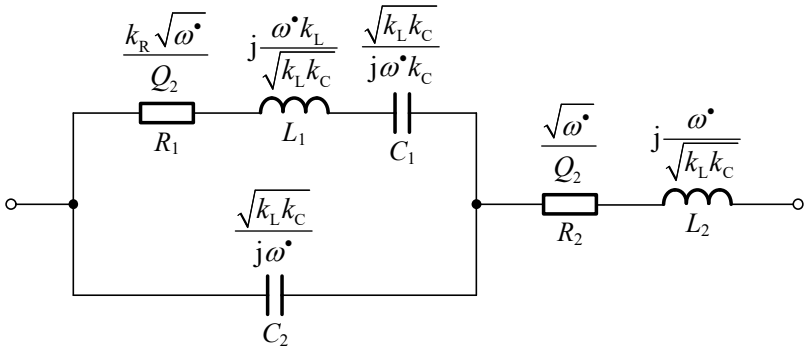

Figure 5. Equivalent diagram of a series-parallel load circuit expressed in relative units related to the characteristic impedance Z_{02}.

Equation (1) allows for plotting the modulus $|Z^\bullet|$ and the phase Θ of the impedance as a function of the normalized angular frequency $\omega^\bullet$ (3). An example is shown in Figure 6 for different values of Q_2. Local impedance minima occur near the angular resonant frequencies of each sub-circuit (3). In addition, four sub-ranges can be distinguished from the considered frequency range: two inductive, II_1, II_2 and two capacitive, I_1, I_2.

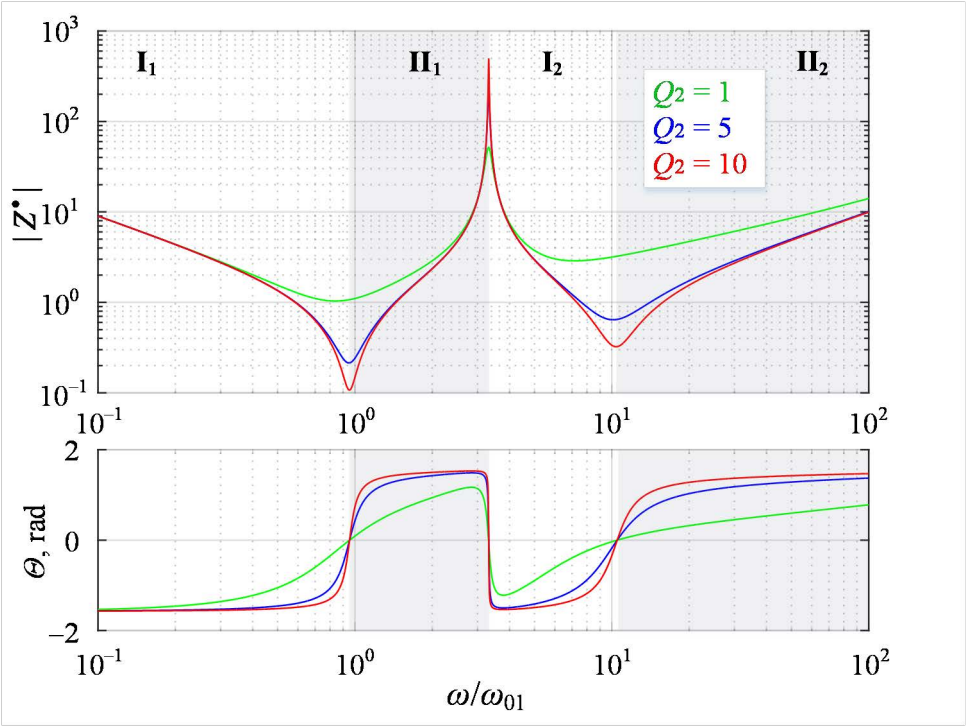

Figure 6. Normalized absolute value and phase of impedance characteristics as a function of normalized angular frequency (k_R = 0.1, k_L = k_C = 10).

A typical power supply for the studied load is a voltage source inverter that generates an output voltage in the form of a square wave. This voltage can be expanded into a Fourier series where its selected normalized harmonic rms value is described by (5). Using (1) and (5), normalized power (6) is determined. The normalized output power $P^\bullet$ is plotted as a function of normalized angular frequency $\omega^\bullet$ at different values of Q_2 in Figure 7. The maximum output power coincides with the occurrence of the impedance minimum values (Figure 6). The power value is much lower for the local maximum located in the higher frequency range. As a result, the power of each component cannot be equally matched. A desirable feature of the induction heating system is the ability to parameterize

the maximum power of each component. This requires the use of independent matching transformers.

$$V^{\bullet}_{(2h-1)\mathrm{RMS}} = \frac{V_{(2h-1)\mathrm{RMS}}}{V_{\mathrm{DC}}} = \frac{2\sqrt{2}}{\pi(2h-1)} \tag{5}$$

$$P^{\bullet} = \sum_{h=1}^{100} \frac{\sqrt{\omega^{\bullet}(2h-1)}}{Q_2} \left(\frac{V^{\bullet}_{(2h-1)\mathrm{RMS}}}{Z^{\bullet}} \right)^2 \tag{6}$$

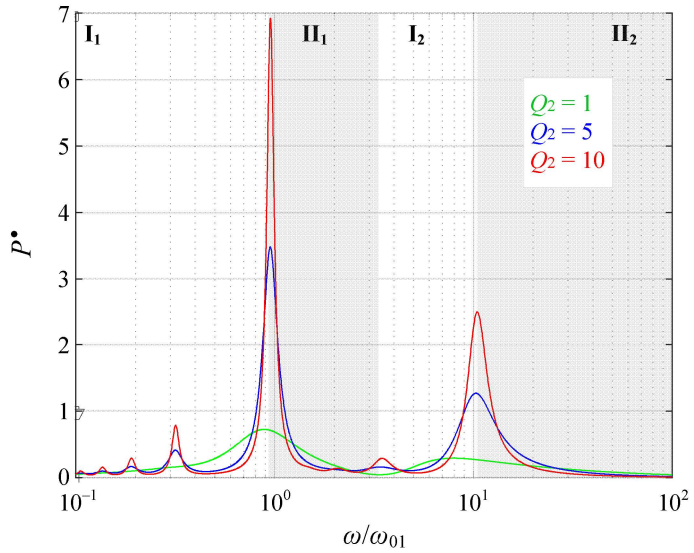

Figure 7. Normalized characteristics of active power as a function of normalized angular frequency (k_R = 0.1, k_L = k_C = 10).

The above simplified model does not consider the nonlinear nature of the ferromagnetic load [27]. To obtain accurate data on the inductor-load circuit, it is necessary to study a specific case using the finite element method (FEM).

4. Power Losses of Converter

The analysis of power losses which is performed in this section is based on manufacturer datasheets and LTspice models provided for semiconductor devices. Two models are simulated. The first one utilizes the internal diode of the tested SiC MOSFET C2M0080120D (Wolfspeed), and the second one has an added external Schottky diode C4D10120A. The LTspice simulation performed is in accordance with IEC60747-8. Switching energies calculated from (7) depend on selecting proper integration limits for the considered case.

$$E_{\mathrm{ON,OFF}} = \int_{t_1}^{t_2} v_{\mathrm{T}}(t) i(t) \mathrm{d}t \tag{7}$$

where v_T and i are the drain-source voltage and current of the transistor, respectively.

In order to validate simulation data, using a curve fitting tool, the $E_{ON,OFF}$ characteristics were extracted from the datasheet for two reference voltages: 600 V and 800 V. Afterwards, for each pair of points for the same current value, the straight line equation was determined. Such a procedure allowed for extrapolation of switching energy for any assumed voltage level. Simulated power losses were lower compared to values extracted from the datasheet.

During the hard-switching operation of the half-bridge, two additional sources of losses should be considered. The first one related to the energy stored in C_{OSS} (8). The second one related to the reverse recovery charge $Q_{RR,C}$ (9).

$$E_{OSS} = \int_0^V v_T C_{OSS}(V_{DC}) \mathrm{d}v_T \tag{8}$$

$$E_{RR} = \frac{Q_{RR,C} V_{DC}}{2} \tag{9}$$

As the external gate resistance R_G increases, the switching times take longer. Therefore, switching energies increase accordingly. The manufacturer provides switching energy characteristics as a function of R_G for 800 V. Referring to the switching energy characteristics determined for R_G = 2.5 Ω discussed above, a correction coefficient is introduced (10).

$$k_{RG} = 0.13 \frac{R_G}{1\Omega} + 0.67 \tag{10}$$

It is valid for any R_G. The estimation was based on the transistor's catalog data, specifically the switching energy characteristics E_{ON} and E_{OFF} as a function of R_G.

Total power losses P_D for a half-bridge are given by (11). Depending on the operating mode, there are selected elements.

$$P_D = 2f[k_{RG}(E_{ON} + E_{OFF}) + E_{RR} + 2E_{OSS}] + I_{RMS}^2 R_{DS(on)} \tag{11}$$

Polynomials approximating the switching energies and value of the worst case on-state resistance (T_j = 150 °C, $i \geq 20$ A) are listed in Table 2. Using these data, the MATLAB model was parameterized. This model consisted of a Simulink model that was iteratively run by an m-file script that aggregated data regarding power losses in the transistor.

Table 2. Losses' calculations parameters for C2M0080120D.

Symbol	Expression	Unit
$E_{ON,\ 330\ V}$	$0.2987 \cdot i^2 - 0.2389 \cdot i + 23.355$	µJ
$E_{OFF,\ 330\ V}$	$-0.0006 \cdot i^4 + 0.0421 \cdot i^3 - 0.7625 \cdot i^2 + 5.2645 \cdot i + 1.5903$	µJ
$E_{ON,\ 600\ V}$	$0.5005 \cdot i^2 + 5.0076 \cdot i + 57.282$	µJ
$E_{OFF,\ 600\ V}$	$-0.0005 \cdot i^4 + 0.0368 \cdot i^3 - 0.6212 \cdot i^2 + 3.911 \cdot i + 14.017$	µJ
$E_{ON,\ 800\ V}$	$0.65 \cdot i^2 + 8.8939 \cdot i + 82.413$	µJ
$E_{OFF,\ 800\ V}$	$-0.0004 \cdot i^4 + 0.0329 \cdot i^3 - 0.5165 \cdot i^2 + 2.9084 \cdot i + 23.222$	µJ
E_{RR}	$76 \cdot 10^{-3} \cdot V_{DC}$	µJ
E_{OSS}	$38.32 \cdot 10^{-6} \cdot V_{DC}{}^2 + 10.94 \cdot 10^{-3} \cdot V_{DC} + 185.2 \cdot 10^{-3}$	µJ
$R_{DS(on)}$	150	mΩ

The individual power loss components of the half-bridge as a function of switching frequency are presented in Figure 8. The calculations are performed for a full-bridge inverter supplied with 800 V, loaded with a series *RLC* circuit. The highlighted red dot represents operation of the converter at nominal power P_N in ZVS, which is desirable due to the reduction of switching power losses. The switching frequency is slightly higher than the resonant frequency of the resonant circuit.

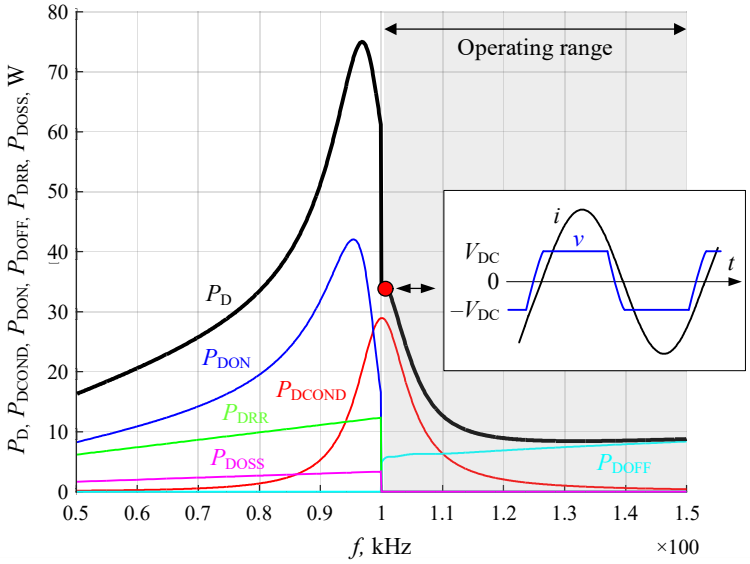

Figure 8. Characteristics of individual components of losses as a function of switching frequency in a half-bridge based on C2M0080120D. Quality factor Q = 10, resonant frequency f_0 = 100 kHz, nominal power P_N = 10 kW at resonance, R_G = 2.5 Ω, DC bus voltage V_{DC} = 800 V.

The developed model allowed for the calculation of characteristics of power losses for C2M0080120D half-bridges, which operate at nominal power in ZVS as a function of nominal power, frequency and DC bus voltage. A family of these characteristics is shown in Figure 9. A general conclusion from the presented characteristics is that for a low value of supply voltage V_{DC} = 330 V, switching losses can be neglected regardless of switching frequency. This is because, regardless of the switching frequency, the total power losses for the C20080120D half-bridge supplied with 330 V are equal to each other (Figure 9a). Conduction losses are dominant in this case. As the voltage increases, switching losses increase as well, and conduction losses decrease. The total losses decrease as a consequence of the voltage increase. Therefore, to achieve minimum losses, it is desirable to supply the maximum voltage at which the inverter can operate properly.

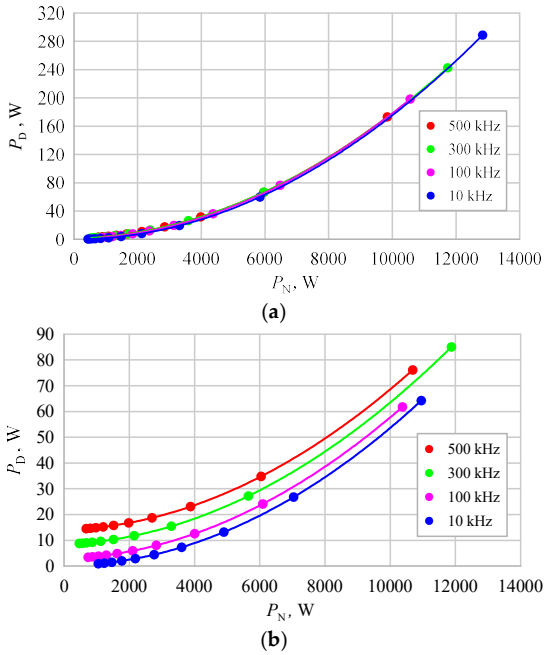

Figure 9. *Cont.*

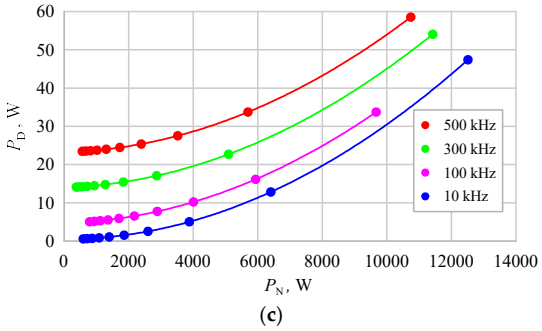

Figure 9. Characteristics of losses' P_D in half-bridge C2M0080120D as a function of nominal power P_N, frequency f and DC bus voltage: (**a**) V_{DC} = 330 V; (**b**) V_{DC} = 600 V; (**c**) V_{DC} = 800 V.

5. Experimental Results

The proposed topologies have been constructed and tested in the laboratory. To provide a comprehensive test, half-bridge modules based on C2M0080120D SiC MOSFETs were constructed, as shown in Figure 10. This approach made it possible to configure the discussed topologies. Moreover, it is even more important that each cooling system is not affected by another. Due to the modular structure, the power losses of each half-bridge were estimated using the steady-state temperature measurement method [28]. This method consists in preliminary scaling of the given losses in the transistor as a function of the measured temperature for the steady state. Then, during operation of the target system, power losses are estimated based on the knowledge of the steady-state temperature. This approach was made possible by using an independent cooling system for each half-bridge. Hence, to confirm results, the power losses are measured as a function of temperature using NTC thermistors.

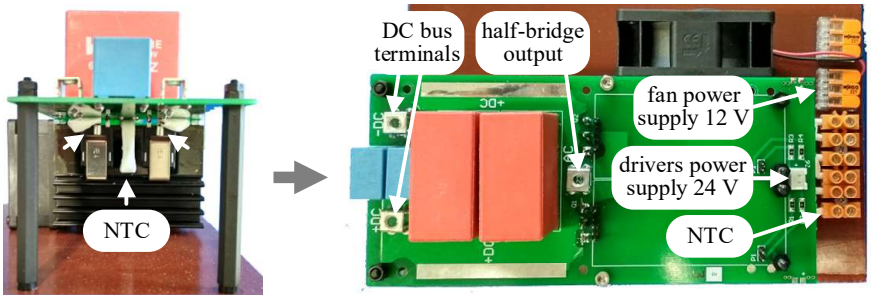

Figure 10. Photographs of half-bridge module based on C2M0080120D.

The load circuit is shown in Figure 11. Depending on the topology implemented, this allows the configuration of the appropriate matching transformers presented in Figure 12. The test bench has a limited power of less than 4 kW. To recreate load conditions similar to a real application (an order of magnitude of the power used in the hardening process), multi-turn inductor was used. Thereupon, the magnetic field acting on the heated ferromagnetic element has been multiplied. This enabled the investigation of the impact of nonlinear load properties on the control of individual components of power. A water cooled ¾ inch steel tube was used as a dummy load.

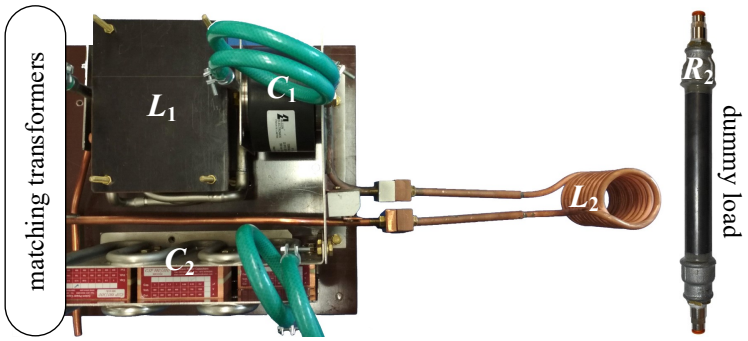

Figure 11. Photograph of the water-cooled resonant load circuit.

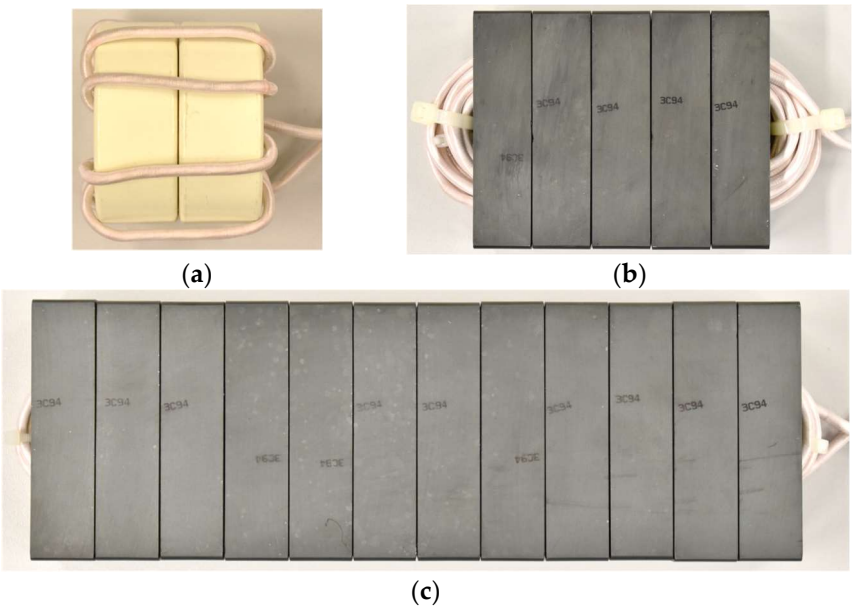

Figure 12. Photograph of matching transformers: (**a**) Tr_2 used for 2T1C and 3T setup 2; (**b**) Tr_1 used for all cases; (**c**) Tr_2 used for 3T setup 1.

The use of two matching transformers allows for setting the power of each component at the desired level. Assuming the use of the proposed topologies as pulsing or simultaneous inverters, it is necessary to use different configurations of matching transformers. For example, in simultaneous operation mode of the 3T topology, the MF voltage component occurs on the primary side of the Tr_2 transformer. Hence, it is necessary to oversize it (Figure 12c). Therefore, the 3T topology was tested for two configurations of the Tr_2 transformer named setup 1 and setup 2. This phenomenon does not occur in the 2T1C topology, where the transformer shown in Figure 12a is used for both operation modes. The turns ratios are summarized in Table 3. Due to the nonlinear nature of the load [27], the turns ratios were selected empirically. The geometry of the core was determined based on the equation for the minimum core cross section [29]. The transformers are roughly designed to allow validation of the conceptual topologies. The authors assume that future research in this area will focus on turns ratios selection and geometric optimization.

Table 3. Configurations of transformers' ratios.

Setup	Operation Mode	Topology	Tr_1	Tr_2
–	pulsing, simultaneous	2T1C	11:1	8:1
1	pulsing, simultaneous	3T	22:1	8:1
2	pulsing	3T	22:1	11:1

The diagram of the test bench is shown in Figure 13. A power analyzer was used to measure input power and components of the output power. The results of experiments presented in Figure 14 show the convergence of the results obtained for two different methods of loss measurement. In the case of 3T, higher losses determined by the thermal method in relation to the power analyzer are observed. The difference is 1 W per transistor, which approximately corresponds to a temperature change of 5 °C. This may be related to some offset error due to ambient temperature deviation.

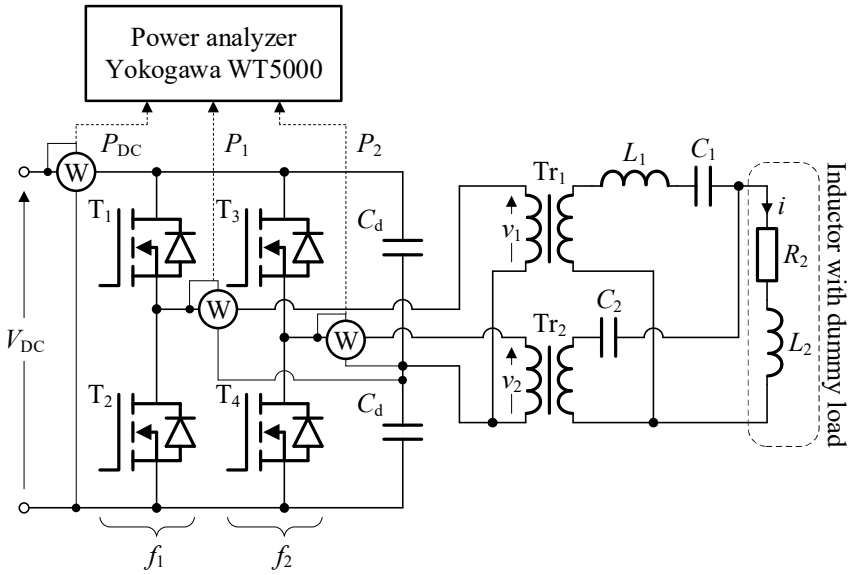

Figure 13. Schema of 2T1C experimental stand. For the 3T topology, the common capacitor C_d branch is replaced with a transistor branch.

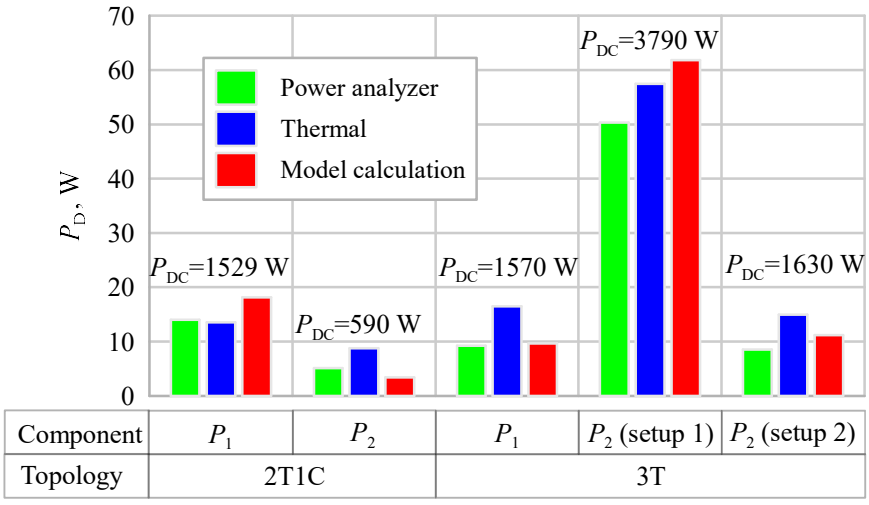

Figure 14. Power losses comparison for pulsing operation mode.

Figure 15 shows the ability of both topologies to independently control the power of each component using frequency modulation. A characteristic feature of the 3T in pulsing operation mode is the full-bridge power supply for both components, which results in twice the inverter output voltage compared to the 2T1C in a similar operation case.

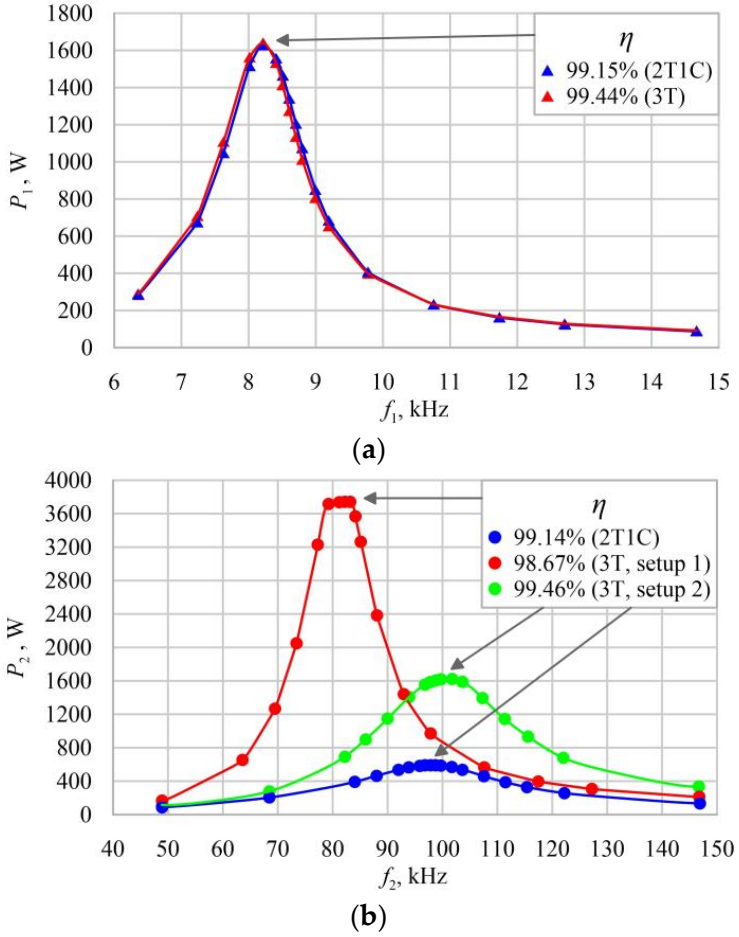

Figure 15. Characteristics of power as a function of frequency in pulsing operation mode: (**a**) MF control mode f_1 = var.; (**b**) HF control mode f_2 = var.

Figure 16 shows power control characteristics for simultaneous operation mode. By analyzing the characteristic in Figure 16a, which describes control of the MF component P_1, change in the HF component P_2 is observed. The change of P_2 is correlated with the change of P_1. In conclusion, P_2 is a function of P_1. A similar effect is not observed in the second case (Figure 16b), which describes control of the HF component P_2. The difference is in the depth of penetration of the MF component, which causes saturation and, at the same time, a decrease in the magnetic permeability of the heated element. This in turn increases penetration depth, thus reducing the equivalent resistance. Therefore, the quality factor for the HF component is increased, resulting in an increase in power. The characteristics shown in Figure 16b demonstrate the ability to independently control the HF component P_2 without affecting the MF component P_1. The decrease in resonant frequency noticed for 3T is due to additional parasitic inductance caused by the oversized transformer (Figure 12c). Moreover, the differences in the nominal power P_2 result from the skin effect. In all cases tested, inverter efficiency η above 97% was achieved. Figures 17 and 18 show waveforms complementary to the presented power characteristics. The measured quantities are marked in Figure 13.

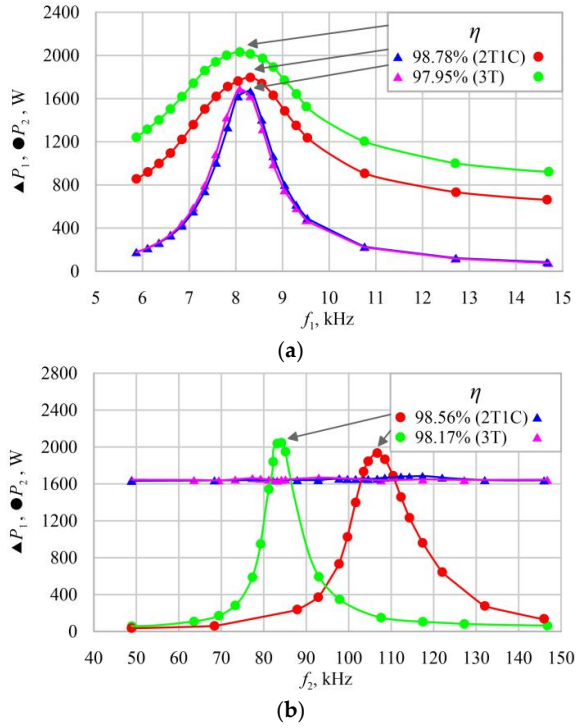

Figure 16. Characteristics of power as a function of frequency in simultaneous operation mode: (**a**) MF control mode f_1 = var., f_2 = const.; (**b**) HF control mode f_1 = const., f_2 = var.

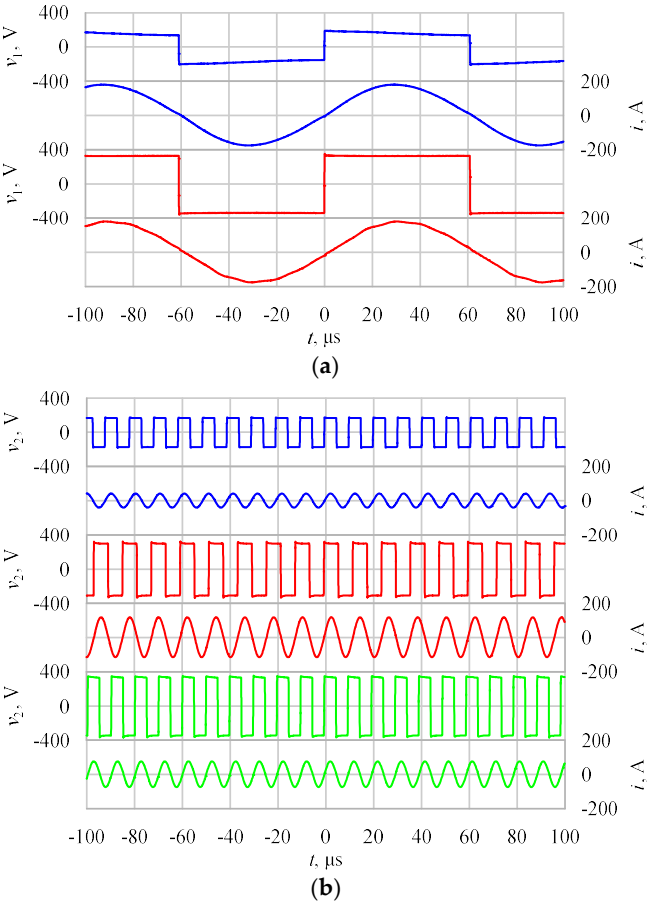

Figure 17. Voltages and currents' waveforms in pulsing operation mode: (**a**) MF; (**b**) HF.

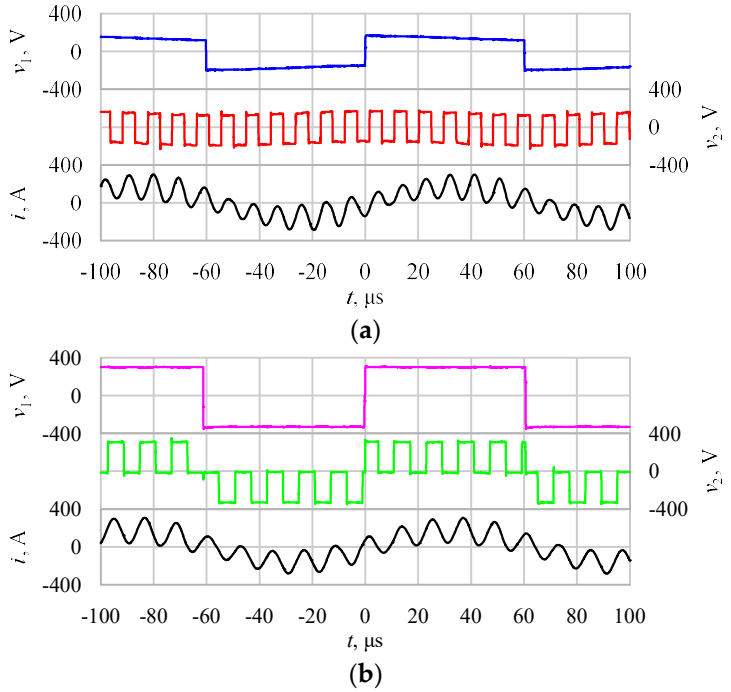

Figure 18. Voltages and currents' waveforms in simultaneous operation mode: (**a**) 2T1C topology; (**b**) 3T topology.

6. Conclusions

New inverter topologies for IH have been introduced and their performance benefits have been analyzed and discussed. A significant problem is the effect of frequency on the load equivalent resistance, which limits the power transfer capability of the HF component. By using two matching transformers for each branch (HF and MF), the effect of frequency on the load equivalent resistance can be compensated. The inverter efficiencies for the proposed 2T1C and 3T systems during pulsing and simultaneous operation achieved values above 98% and 97%, respectively.

7. Patents

Patents resulting from the work reported in this manuscript [25,26].

Author Contributions: Conceptualization, K.F. and K.K.; methodology, K.F. and K.K.; software, K.K.; validation, K.F. and K.K.; formal analysis, K.F. and K.K.; investigation, K.F. and K.K.; resources, M.K. and P.Z.; data curation, K.K.; writing—original draft preparation, K.F., K.K., M.K. and P.Z.; writing—review and editing, K.F., K.K., M.K. and P.Z.; visualization, K.F.; supervision, K.F.; project administration, K.F.; funding acquisition, K.F. All authors have read and agreed to the published version of the manuscript.

Funding: This research was funded by the Excellence Initiative—Research University program implemented at the Silesian University of Technology, grant number 05/050/SDU/10-22-02.

Data Availability Statement: The data presented in this study are available on request from the corresponding author.

Conflicts of Interest: Author Kamil Kierepka was employed by the company TRUMPF Huettinger. Author Piotr Zimoch was employed by the company TechFirm Industrie AG. The remaining authors declare that the research was conducted in the absence of any commercial or financial relationships that could be construed as a potential conflict of interest.

References

1. Mühlbauer, A. *History of Induction Heating and Melting*; Vulkan-Verlag: Essen, Germany, 2008.
2. Hofmann, C.; Kroll, M.; Panhale, S.; Wiemer, M.; Kunke, A.; Hiller, K.; Kuhn, H. Inductive Heating Based on VHF-ISM Radio Band Frequencies as Technology Platform for Efficient Heating of Metallic Micro-Scaled Bonding Layers in MEMS Packaging. *IEEE Trans. Magn.* **2023**, *59*, 2800905. [CrossRef]
3. Wang, B.; Mingyin, Y. Research on the Improvement of Lithium-Ion Battery Performance at Low Temperatures Based on Electromagnetic Induction Heating Technology. *Energies* **2023**, *16*, 7780. [CrossRef]
4. Esteve, V.; Jordan, J.; Dede, E.J.; Sanchis-Kilders, E.; Martinez, P.J.; Maset, E.; Gilabert, D. Optimal LLC Inverter Design with SiC MOSFETs and Phase Shift Control for Induction Heating Applications. *IEEE Trans. Ind. Electron.* **2022**, *69*, 11100–11111. [CrossRef]
5. Pascual, A.; Acero, J.; Carretero, C.; Llorente, S.; Burdio, J. Electromagnetic Modeling and Analysis of Multimaterial Cookware for Domestic Induction Heating. *IEEE Access* **2023**, *11*, 79275–79284. [CrossRef]
6. Sezer, C.; Altintas, N. Adaptation of Inductive Power Transfer to Small Household Appliances That Can Operate on Induction Heating Cooktops: Wireless Electric Kettle. *Energies* **2023**, *16*, 3544. [CrossRef]
7. Zungor, F.; Bodur, H.; Ozturk, M.; Obdan, H. Design Methodology of Series Resonant Half Bridge Inverter for Induction Cooker. *IEEE Access* **2023**, *11*, 135476–135492. [CrossRef]
8. Lodi, M.B.; Makridis, A.; Kazeli, K.; Samaras, T.; Angelakeris, M.; Mazzarella, G.; Fanti, A. On the Evaluation of the Hyperthermic Efficiency of Magnetic Scaffolds. *IEEE Open J. Eng. Med. Biol.* **2023**, *5*, 88–98. [CrossRef] [PubMed]
9. Prantner, M.; Parspour, N. Eddy Current Heating of Implanted Devices for Tumor Ablation: Numerical-Analytic Analysis and Optimization. *IEEE Access* **2023**, *11*, 52088–52100. [CrossRef]
10. Chang, C.-J.; Tai, C.-C.; Lin, F.-W.; Kuo, C.-C.; Hung, C.-M. Effects of Flexible Induction Coil Pitch on the Heating Performance of Thermotherapy Needles. *IEEE Trans. Instrum. Meas.* **2020**, *69*, 8983–8991. [CrossRef]
11. Plumed, E.; Lope, I.; Acero, J. Induction Heating Adaptation of a Different-Sized Load With Matching Secondary Inductor to Achieve Uniform Heating and Enhance Vertical Displacement. *IEEE Trans. Power Electron.* **2021**, *36*, 6929–6942. [CrossRef]
12. Pham, H.N.; Fujita, H.; Ozaki, K.; Uchida, N. Estimating Method of Heat Distribution Using 3-D Resistance Matrix for Zone-Control Induction Heating Systems. *IEEE Trans. Power Electron.* **2012**, *27*, 3374–3382. [CrossRef]
13. Egalon, J.; Caux, S.; Maussion, P.; Souley, M.; Pateau, O. Multiphase System for Metal Disc Induction Heating: Modeling and RMS Current Control. *IEEE Trans. Ind. Appl.* **2012**, *48*, 1692–1699. [CrossRef]
14. Pascual, A.; Acero, J.; Llorente, S.; Carretero, C.; Burdio, J.M. Small-Sized Immersible Water Heaters for Domestic Induction Heating Technology. *IEEE Access* **2023**, *11*, 51480–51489. [CrossRef]
15. Rudnev, V.; Loveless, D.; Cook, R.; Black, M. Induction Hardening of Gears: A Review. Part 1. *Heat Treat. Met.* **2003**, *4*, 97–103.
16. Rudnev, V.; Loveless, D.; Cook, R.; Black, M. Induction Hardening of Gears: A Review. Part 2. *Heat Treat. Met.* **2004**, *1*, 11–15.
17. Schwenk, W.; Häussler, A.; Heiliger, A. Einrichtung zum induktiven Erwärmen von Werkstücken. Patent EP1363474B1, 16 April 2003.
18. Esteve, V.; Jordan, J.; Dede, E.J.; Magraner, J.M.; Cases, C. Inductive Heating Converter Comprising a Resonant Circuit with Simultaneous Multi-Frequency Current Output and at Least Two Inverters. Patent EP2147983A1, 21 July 2008.
19. Dede, E.J.; Esteve, V.; Jordan, J.; Cases, C.; Magraner, J.M. Inductive Heating Apparatus Comprising a Resonant Circuit with Simultaneous Dual Frequency Current Output and a Single Inverter Circuit with Silicon Carbide. Patent EP2148551A1, 21 July 2008.
20. Esteve, V.; Pardo, J.; Jordan, J.; Dede, E.J.; Sanchis-Kilders, E.; Maset, E. High Power Resonant Inverter with Simultaneous Dual-Frequency Output. In Proceedings of the IEEE 36th Power Electronics Specialists Conference, Dresden, Germany, 16 June 2005; pp. 1278–1281.
21. Esteve, V.; Jordan, J.; Dede, E.J.; Sanchis-Kilders, E.; Maset, E. Induction Heating Inverter with Simultaneous Dual-Frequency Output. In Proceedings of the Twenty-First Annual IEEE Applied Power Electronics Conference and Exposition, Dallas, TX, USA, 19–23 March 2006; pp. 1505–1509.
22. Esteve, V.; Jordan, J.; Sanchis-Kilders, E.; Dede, E.J.; Maset, E.; Ejea, J.B.; Ferreres, A. Comparative Study of a Single Inverter Bridge for Dual-Frequency Induction Heating Using Si and SiC MOSFETs. *IEEE Trans. Ind. Electron.* **2015**, *62*, 1440–1450. [CrossRef]
23. Sarnago, H.; Lucia, O.; Burdio, J.M. Multiresonant Power Converter for Improved Dual-Frequency Induction Heating. *IEEE Trans. Power Electron.* **2019**, *34*, 2097–2103. [CrossRef]
24. Zgraja, J. Dual-Frequency Induction Heating Generator with Adjustable Impedance Matching. *IEEE Trans. Ind. Electron.* **2019**, *66*, 8308–8317. [CrossRef]
25. Kierepka, K.; Frania, K.; Kasprzak, M.; Zimoch, P. Double-Frequency Induction Heating Device with 3-Phase Voltage Inverter with Half Capacitor Bridge. Patent PL241666B1, 25 April 2022.
26. Kierepka, K.; Frania, K.; Kasprzak, M.; Zimoch, P. Device for Two-Frequency Induction Heating with a 3-Phase Voltage Inverter. Patent PL439134A1, 9 May 2022.
27. Rudnev, V.; Loveless, D.; Cook, R. *Handbook of Induction Heating*; CRC Press: Boca Raton, FL, USA, 2017.

28. Zhang, X.; Feng, Z.; Wang, J.; Yu, S. An Optimized Temperature Sensor Calorimetric Power Device Loss Measurement Method. *Energies* **2019**, *12*, 1333. [CrossRef]
29. Kazimierczuk, M.K. *High-Frequency Magnetic Components*; Wiley: Hoboken, NJ, USA, 2014.